ACS APPLIED MATERIALS & INTERFACES

Research Article

www.acsami.org

Carbon-Armored Co_9S_8 Nanoparticles as All-pH Efficient and Durable H_2-Evolving Electrocatalysts

Liang-Liang Feng,[†] Guo-Dong Li,[†] Yipu Liu,[†] Yuanyuan Wu,[†] Hui Chen,[†] Yun Wang,[†] Yong-Cun Zou,[†] Dejun Wang,[†,‡] and Xiaoxin Zou*[,†]

[†]State Key Laboratory of Inorganic Synthesis and Preparative Chemistry, College of Chemistry, Jilin University, 2699 Qianjin Street, Changchun, Jilin 130012, China

[‡]Department of Chemistry, Tsinghua University, Beijing 100084, China

Supporting Information

ABSTRACT: Splitting water to produce hydrogen requires the development of non-noble-metal catalysts that are able to make this reaction feasible and energy efficient. Herein, we show that cobalt pentlandite (Co_9S_8) nanoparticles can serve as an electrochemically active, noble-metal-free material toward hydrogen evolution reaction, and they work stably in neutral solution (pH 7) but not in acidic (pH 0) and basic (pH 14) media. We, therefore, further present a carbon-armoring strategy to increase the durability and activity of Co_9S_8 over a wider pH range. In particular, carbon-armored Co_9S_8 nanoparticles (Co_9S_8@C) are prepared by direct thermal treatment of a mixture of cobalt nitrate and trithiocyanuric acid at 700 °C in N_2 atmosphere. Trithiocyanuric acid functions as both sulfur and carbon sources in the reaction system. The resulting Co_9S_8@C material operates well with high activity over a broad pH range, from pH 0 to 14, and gives nearly 100% Faradaic yield during hydrogen evolution reaction under acidic (pH 0), neutral (pH 7), and basic (pH 14) media. To the best of our knowledge, this is the first time that a transition-metal chalcogenide material is shown to have all-pH efficient and durable electrocatalytic activity. Identifying Co_9S_8 as the catalytically active phase and developing carbon-armoring as the improvement strategy are anticipated to give a fresh impetus to rational design of high-performance noble-metal-free water splitting catalysts.

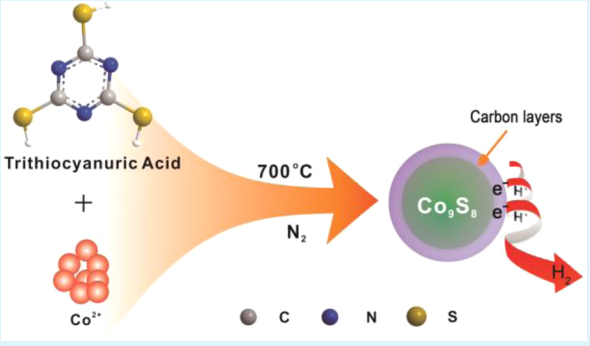

KEYWORDS: *water splitting, hydrogen evolution, carbon, cobalt, sulfide*

INTRODUCTION

Sustainable production of hydrogen, a clean-burning fuel, from abundant and easily accessible resources (e.g., water) is an appealing, but challenging, task in science today. One of the compelling visions for sustainable hydrogen production is water electrolysis using solar- or wind-derived electricity.[1] This process requires the development of new catalytic materials that are able to make water splitting energy efficient. Up to now, Pt-based metals have been found to be effective toward the hydrogen evolution reaction (HER), but their widespread use as catalysts is limited by their high cost and scarcity in nature. Hence, sustained and focused efforts have recently been devoted to finding suitable non-noble-metal catalysts that are composed of earth-abundant elements and have high catalytic activity.[2−4] There are now a number of successful examples of such noble-metal-free HER catalysts with activities close to that of Pt. Among them, transition metal chalcugenides are a family of promising materials to replace Pt as the next-generation HER catalysts. Nørskov's group first showed that MoS_2 nanoparticles functioned as an active HER catalyst.[5] After this pioneering work, there were several studies on the identification of MoS_2's active sites and the improvement of MoS_2's catalytic performances by various structural modification methods.[6−10] In addition, some crystalline transition metal chalcogenides with a new composition, such as WS_2,[11,12] CoS_2,[13−15] $CoSe_2$,[16,17] and FeS,[18] were reported recently to be non-Pt HER catalysts. Besides those crystalline compounds, amorphous Mo- or Co-based sulfides were also successfully prepared by (electro)chemical methods, and they were shown to have the ability to electrocatalytically reduce water.[19,20]

All the above-mentioned studies, meanwhile, demonstrated that composition and structures (including crystal structure and micronano structure) of the HER catalysts played critical roles in determining not only the material's catalytic efficiency but also the reaction conditions we finally use. For example, Mo/W-based chalcogenides generally only work well toward HER in acidic media[6−12] but have much lower catalytic activity or unstability in neutral and basic media. In addition, CoS_2 and $CoSe_2$ prefer acidic media,[13−17] whereas the electrochemically deposited amorphous CoS_x material is only highly active in

Received: November 10, 2014
Accepted: December 23, 2014
Published: December 23, 2014

DOI: 10.1021/am507811a
ACS Appl. Mater. Interfaces 2015, 7, 980−988

neutral media.[20] This preference of a given HER catalyst in terms of reaction condition, intrinsically, is related to the pH-dependent (electro)chemical stability and/or catalytic mechanism of the chalcogenide material. Despite some achievements made in the field of chalcugenide HER catalysts, as outlined above, there were no reports on a transition-metal chalcogenide material that has efficient and durable catalytic performance at all pH values (pH 0−14).

Herein, we report the synthesis of carbon-armored Co_9S_8 nanoparticles (Co_9S_8@C) that can work well with high activity over a broad pH range from pH 0 to 14, although the pristine Co_9S_8 is unstable in acidic and basic media. The importance of this work mainly lies in (i) identifying Co_9S_8 as a new catalytically active phase and (ii) developing carbon-armoring as a viable performance improvement strategy. In addition, designing all-pH efficient HER catalysts is of scientific importance because this will (i) provide the potential to easily couple the HER catalysts with the OER catalysts (which mediate the oxygen evolution reaction, the other half reaction of the water splitting reaction) in a single water-splitting system regardless of pH[21,22] and (ii) also allow one to apply them to different types of water electrolysis technologies (e.g., proton exchange membrane-based electrolysis cell, acidic condition;[23,24] microbial electrolysis cell, neutral condition;[25] and alkaline electrolysis cell, basic condition).[26] Furthermore, although Co_9S_8 has been used as the catalyst for the hydrodesulphurization reaction[27,28] and oxygen reduction reaction[29,30] and as electrode materials in the dye-sensitized solar cell,[31−34] supercapacitor,[35,36] elctrochemical hydrogen storage,[37] and lithium-ion battery previously,[38−42] this is the first time that Co_9S_8 is reported to catalyze HER effectively.

EXPERIMENTAL SECTION

Chemicals and Reagents. Trithiocyanuric acid was purchased from Aladdin Industrial Corporation. Thiourea was purchased from Tianjin Fuchen Chemical Reagents Factory. Cobalt(II) nitrate hexahydrate, cobalt(II) acetate tetrahydrate, and iron(III) nitrate nonahydrate were purchased from Xilong Chemicals Co., Ltd.. Dipotassium hydrogen phosphate (K_2HPO_4), potassium dihydrogen phosphate (KH_2PO_4), sulfuric acid (H_2SO_4), potassium hydroxide (KOH), and ethylene glycol were purchased from Beijing Chemical Factory. Highly purified water (>18 MΩ cm resistivity) was provided by a PALL PURELAB Plus system.

Synthesis of Co_9S_8@C. Trithiocyanuric acid (1.13 mmol) was mixed with cobalt(II) nitrate hexahydrate (0.34 mmol), and then, the homogeneous mixture was placed on a quartz boat in a tube furnace in N_2 atmosphere. The temperature in the furnace was raised from room temperature to 700 °C at a ramp of 10 °C/min and kept at 700 °C for 3 h. For comparative studies, two more samples were prepared by heating the same precursor mixture in N_2 atmosphere at varying temperature (600 or 800 °C) for 3 h. In addition, iron(III) nitrate nonahydrate was also used to replace cobalt(II) nitrate hexahydrate in the reaction system to prepare iron-based sulfide/carbon composite material.

Synthesis of Co_9S_8 Nanoparticles. Cobalt(II) acetate tetrahydrate (5 mmol) and thiourea (5 mmol) were dissolved in ethylene glycol (30 mL), and then, the resulting solution was placed in a Teflon-lined stainless steel autoclave (40 mL) and maintained at 200 °C in an oven for 8 h. After cooling down to room temperature, the solid powders in the reaction system were collected and dried at 60 °C for 6 h.

General Characterization. The powder X-ray diffraction (XRD) patterns were recorded on a Rigaku D/Max 2550 X-ray diffractometer with Cu Kα radiation (λ = 1.5418 Å). The X-ray photoelectron spectroscopy (XPS) was performed on an ESCALAB 250 X-ray photoelectron spectrometer with a monochromatic X-ray source (Al Kα $h\nu$ = 1486.6 eV). The Raman spectra were obtained with a Renishaw Raman system model 1000 spectrometer with a 20 mW air-cooled argon ion laser (514.5 nm) as the exciting source. The transmission electron microscope (TEM) images were obtained with a Philips-FEI Tecnai G2S-Twin microscope equipped with a field emission gun operating at 200 kV. The scanning electron microscope (SEM) images were obtained with a JEOL JSM 6700F electron microscope. To determine the amount of carbon in the sample, thermogravimetric analysis (TGA) was performed using with a NETZSCH STA 449C TG thermal analyzer by heating the samples from 25 to 950 °C at a heating rate of 10 °C/min in air. The evolved gases were detected by a gas chromatograph (Shimadzu, GC-2014C with a thermal conductivity detector, Molecular sieve 5 Å, Argon gas). The ICP-OES elemental analyses were performed on a PerkinElmer Optima 3300DV ICP spectrometer.

HER Measurements. The electrocatalytic properties were studied with a three-electrode system using a CH Instrument (Model 650E). A similar method was also used in our previous reports.[21,22] The reference electrode was a saturated calomel electrode (SCE), and the counter electrode was a carbon rod. We prepared the working electrode by following the steps below: (i) the catalyst (2 mg) was dispersed in isopropanol (200 μL) to form a homogeneous mixture under sonication; (ii) this solution (2 μL) was drop-casted onto a glassy carbon electrode (GCE), giving a catalyst loading of c.a. 0.3 mg/cm^2 on the GCE; and (iii) a small amount of Nafion solution was drop-casted on top to protect the catalyst film. For electrochemical measurements, we used 0.5 M H_2SO_4 (pH 0), 1 M phosphate buffer (pH 7), or 1 M KOH (pH 14) as the electrolyte. The scan rate was set to be 50 mV/s in linear sweep voltammetry (LSV) measurements. To get the dependence of current density on the applied voltage as well as Tafel plots, steady-state current density as a function of voltage was measured with a dwell time of 5 min. According to the equation, $E_{vs\ RHE} = E_{vs\ SCE} + E_{o\ SCE} + 0.059pH$, we converted the potential, which was measured against a SCE electrode, into the potential versus the reversible hydrogen electrode (RHE).

RESULTS AND DISCUSSION

Synthesis and Characterization of Co_9S_8@C. For the synthesis of carbon-armored Co_9S_8 nanoparticles (Co_9S_8@C), cobalt nitrate and trithiocyanuric acid were chosen as the starting materials. Trithiocyanuric acid functions as both sulfur and carbon sources in the reaction system. As shown in Figure 1, the Co_9S_8@C material was easily prepared through directly

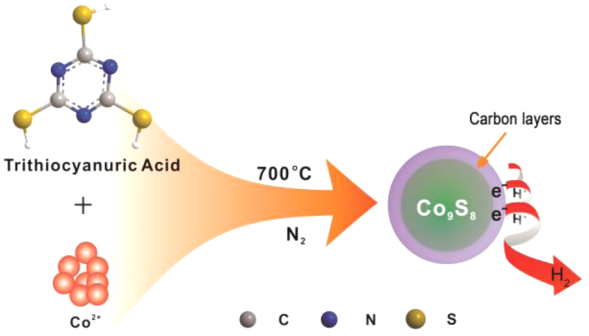

Figure 1. Schematic representation of the synthesis of Co_9S_8@C by direct thermal treatment of a mixture of cobalt(II) nitrate hexahydrate and trithiocyanuric acid at 700 °C in N_2 atmosphere.

heating a mixture of cobalt nitrate and trithiocyanuric acid at 700 °C in a nitrogen atmosphere (the experimental details are provided in the Experimental Section). Note that the reaction temperature (700 °C) plays an important role in the formation of the Co_9S_8@C material (Figure S1 in the Supporting Information). When the reaction temperature was decreased

DOI: 10.1021/am507811a
ACS Appl. Mater. Interfaces 2015, 7, 980−988

to 600 °C, CoS as the impurity phase was observed; whereas when the reaction temperature was increased to 800 °C, metallic cobalt as the impurity phase was detected. Furthermore, a pristine Co_9S_8 sample (denoted hereafter as Co_9S_8) without the carbon protective layer was prepared hydrothermally at 200 °C, and this sample was also carefully characterized for comparative purposes.

Figure 2A shows the XRD patterns of Co_9S_8@C and Co_9S_8. The XRD patterns of the two samples appear very similar, and

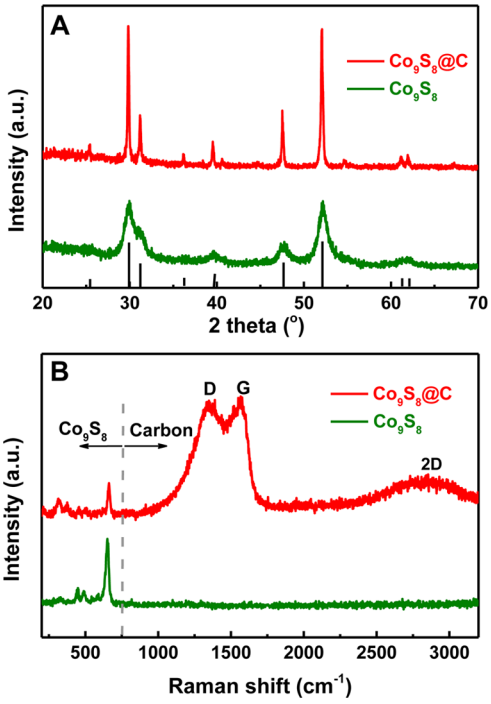

Figure 2. (A) XRD patterns and (B) Raman spectra of Co_9S_8@C and Co_9S_8.

they are indexed as cobalt pentlandite (i.e., Co_9S_8; PDF#65-6801). Comparison of the XRD patterns revealed the stronger diffraction peaks for Co_9S_8@C with respect to Co_9S_8. This demonstrates that Co_9S_8@C has a larger particle size than Co_9S_8 (see TEM characterization below), and this can be explained by the fact that Co_9S_8@C is synthesized at a higher synthesis temperature (700 °C for Co_9S_8@C; 200 °C for Co_9S_8). In addition, no XRD peaks related to graphitic carbon was observed in the XRD pattern of Co_9S_8@C, indicating that the carbon protective layer in Co_9S_8@C should be amorphous.

Figure 2B shows the Raman spectra of Co_9S_8@C and Co_9S_8. As revealed in Figure 2B, the Raman spectrum for Co_9S_8@C can be divided into two parts: <750 cm^{-1} and >750 cm^{-1}. A set of weak Raman bands (<750 cm^{-1}), which are perfectly indexed to Co_9S_8,[43] appear in the spectrum. When the wavenumber is larger than 750 cm^{-1}, the Raman bands related to carbon are only observed for Co_9S_8@C, clearly demonstrating that Co_9S_8@C is a Co_9S_8/carbon composite material (see Raman spectrum of pure carbon in Figure S2 in the Supporting Information). The Co_9S_8@C material exhibits the Raman bands related to carbon, including D, G, and 2D bands.[21,22] The strong D band indicates that a large number of defects or disordered sites are present in the carbon structure of Co_9S_8@C. A large amount of structural defects in Co_9S_8@C is in agreement with the amorphous feature of carbon in it. In addition, the structural defects might also be further caused by the N and S dopants in the carbon structure of Co_9S_8@C (see below).

To evaluate the amount of carbon in Co_9S_8@C, the thermogravimetric (TG) analysis for Co_9S_8@C was carried out in air from 25 to 950 °C, and the corresponding TG curve is shown in Figure 3A. The Co_9S_8@C material is almost stable at temperatures below 200 °C. With the increase in the testing temperature, an obvious weight increase takes place at 250 °C and ends at about 800 °C. This weight increase is mainly attributed to the part oxidation of Co_9S_8 into cobalt sulfate (Figure 3B). When the testing temperature is higher than 900 °C, the weight becomes constant and the product is confirmed to be Co_3O_4 (Figure 3C). During the whole measurement range, the total weight loss is about 18.5%. From this final weight loss value, we estimated that the amount of carbon in Co_9S_8@C is about 10.1 wt %.

The morphology and microstructure of Co_9S_8@C were further characterized by using transmission electron microscopy (TEM). As revealed in Figures 4A,B and S3 in the Supporting Information, some Co_9S_8 nanoparticles with a size of ~50 nm are embedded in the carbon matrix (gray background). The particle size of Co_9S_8@C is obviously larger than that (<5 nm) of hydrothermally prepared Co_9S_8, as demonstrated by the TEM image of Co_9S_8 (Figure S4 in the Supporting Information). This result is in agreement with that obtained through XRD comparison (Figure 1). The high resolution TEM (HRTEM) images of the edge of the Co_9S_8@C material (Figures 4B and S3 in the Supporting Information) show a darker region at the center and a continuous lighter region (2–5 nm) around the edges of the Co_9S_8@C nanoparticles, indicating the presence of a Co_9S_8 core surrounded by the carbon layers (or Co_9S_8/C core/shell type nanoparticles). The different shades of colors observed in the TEM images of the Co_9S_8@C nanoparticles (Figures 4B and S3 in the Supporting Information) are due to the atomic mass difference (Z-contrast) between Co_9S_8 and carbon substrate. An energy-dispersive spectroscopy (EDS) line profile for a typical Co_9S_8@C nanoparticle (Figure 4B, inset) further confirmed that the Co_9S_8 nanoparticle is totally coated by the carbon layer. Moreover, elemental-mapping of the Co_9S_8@C material (Figure 4C–F) shows that all the elements, i.e., C, N, S, and Co, are homogeneously distributed over the entire Co_9S_8@C nanoparticle. This provides a new evidence for the formation of carbon-coated Co_9S_8 nanoparticles. This result also indicates that the carbon layer in Co_9S_8@C might be doped by nitrogen and sulfur. That is a reasonable speculation because trithiocyanuric acid, the starting material for the synthesis of Co_9S_8@C, is composed of C, N, and S elements.

In order to verify that all Co_9S_8 nanoparticles are coated by the carbon protective layer for the Co_9S_8@C material, we treated this material with a strong acid (0.5 M H_2SO_4) at room temperature for 24 h. For comparison, the pristine Co_9S_8 was also treated by acid. As shown in Figure 4G, after acid treatment, the solution for pristine Co_9S_8 is pinkish, while the solution for Co_9S_8@C remains colorless. This results indicates that the Co leaching takes place for pristine Co_9S_8, rather than Co_9S_8@C. The presence/absence of Co^{2+} in the solutions was also confirmed by ICP-OES analysis. These results demonstrate that Co_9S_8 nanoparticles with a low chemical stability in acid are encapsulated inside the carbon shells, and thus, they are not accessible to the strong acid and exhibit a remarkable chemical stability.

DOI: 10.1021/am507811a
ACS Appl. Mater. Interfaces 2015, 7, 980–988

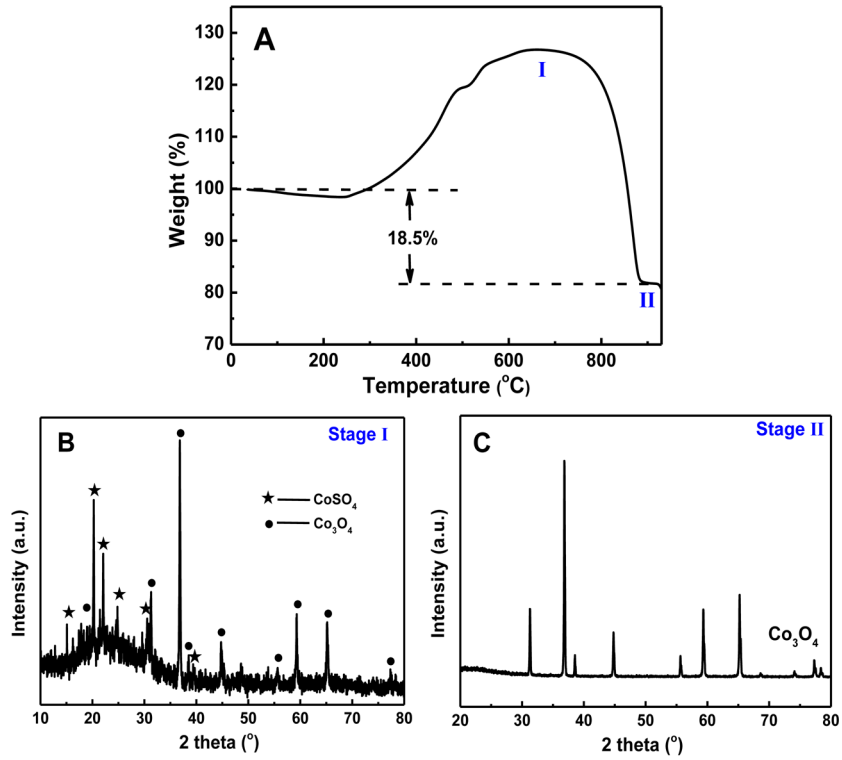

Figure 3. (A) TG curve measured in air from 25 to 950 °C; (B) XRD pattern of the sample that was collected at 800 °C (Stage I); and (C) XRD pattern of the sample that was collected at 950 °C (Stage II).

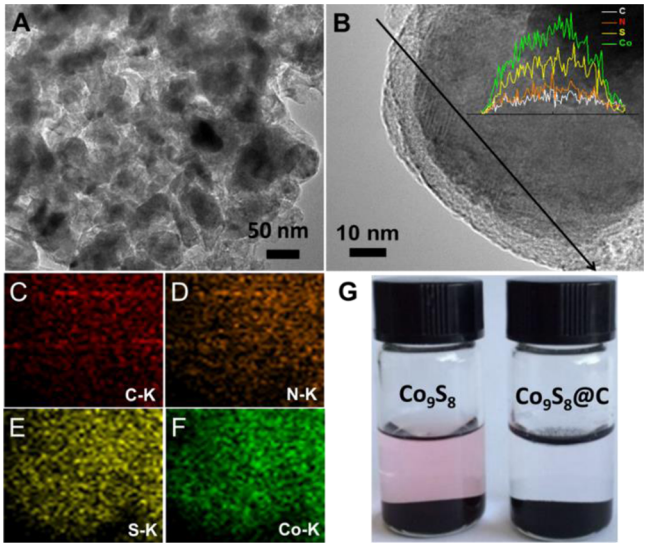

Figure 4. (A, B) TEM images; (C–F) the corresponding elemental mapping images of Co_9S_8@C; and (G) comparison of the chemical stabilities in 0.5 M H_2SO_4 for 24 h of Co_9S_8@C versus Co_9S_8. The inset in (B) shows the corresponding energy-dispersive spectroscopy (EDS) line profile (elemental mapping, black arrow).

X-ray photoelectron spectroscopy (XPS) was performed to obtain the composition information on the carbons in the Co_9S_8@C material as well as the nature of dopants in them. The high resolution C 1s spectrum of Co_9S_8@C (Figure 5A) shows the presence of C═C–C (284.6 eV), C–S (284.9 eV), and C–N (285.8 eV) carbons, as well as O-attached carbons due to the observation of C═O (288.1 eV) and C–O (285.8 eV) signals.[44] The XPS peaks associated with C–N and C–S moieties should be due to the substitution of C atoms with N and S atoms in the carbon matrix, respectively, and the peaks corresponding to C═O and C–O carbons are indicative of the presence of –C–OH and –C–OOH species in the material. In the N 1s XPS spectrum (Figure 5B), the N 1s peak was deconvoluted into three peaks corresponding to three different types of N species including pyridinic (398.7 eV), quaternary (401.0 eV), and pyrrolic (400.1 eV) N species.[44,45] In the S 2p XPS spectrum, the raw curve was peak-fitted into four curves corresponding to three different types of sulfur species.[42,44] The peaks at 162.5 and 161.5 eV are attributable to the 2p1/2 and 2p3/2 core levels of S^{2-} in Co_9S_8, respectively. The peaks at 163.6 and 168.7 eV are assigned to the C–S–C and SO_4^{2-} sulfur, respectively. The presence of C–S–C demonstrated that a certain amount of sulfur is doped in the lattice of carbon matrix, whereas the existence of SO_4^{2-} indicates the sulfur species on the material's surface is partly oxidized by air. Further quantitative analysis of the XPS results reveals that the atomic ratios of N/C and S/N in the carbons of Co_9S_8@C are about 10:100 and 2:100, respectively. Thus, it is concluded that the carbon matrix in the Co_9S_8@C material is defect-rich and contains a large amount of heteroatoms (i.e., nitrogen and sulfur dopants) in it.

HER Activities of Co_9S_8@C. In view of the fact that Co_9S_8 is not chemically stable enough in strong acid (see Figure 4G) and basic media, we first investigated the catalytic activities toward HER of Co_9S_8@C and Co_9S_8 in phosphate buffer solution (pH 7). This was carried out by depositing the samples on a glassy carbon electrode (GCE), which was used as the working electrode in a typical three-electrode system (see Experimental section for details). For comparison, the electrocatalytic activity of 5 wt % Pt nanoparticles on activated carbon (Pt/C) was also measured. To exactly determine the catalytic activities of the materials, we measured their steady-state

DOI: 10.1021/am507811a
ACS Appl. Mater. Interfaces 2015, 7, 980–988

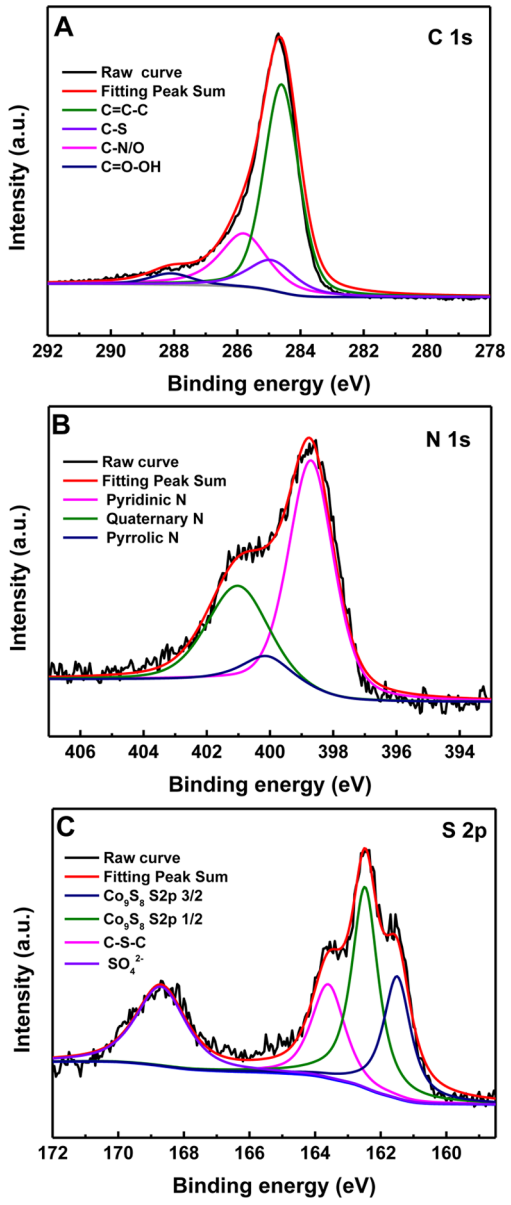

Figure 5. High-resolution (A) C 1s, (B) N 1s, and (C) S 2p XPS spectra for the Co_9S_8@C material.

current densities at various applied voltages with a dwell time of 5 min in phosphate buffer (pH 7).

As shown in Figure 6A, the blank GCE only produces a very weak current even when the potential is increased to −0.6 V vs RHE. In sharp contrast, the Co_9S_8@C and Co_9S_8 materials give significant cathodic currents in neutral solution. After measurement, H_2 bubbles were observed on the cathode surface and H_2 was directly confirmed by gas chromatography (Figure S5 in the Supporting Information). Co_9S_8@C exhibits a small onset potential at −150 mV for HER (the overpotential required to yield a current density of 1 mA/cm^2), beyond which the cathodic current rises rapidly under more negative potentials. Additionally, Co_9S_8@C affords a current density of 10 mA/cm^2 (which is the current density expected for a 10% efficient solar water-splitting device) at a small overpotential (η) of 280 mV, whereas pristine Co_9S_8 gets the same current density at η = 340 mV. This result demonstrates the superior activity of Co_9S_8@C toward HER relative to pristine Co_9S_8.

First, the difference of these two materials' catalytic activities do not correlate with the materials' surface areas, as the BET surface area of Co_9S_8@C is 13 m^2/g and that of Co_9S_8 is 20.3 m^2/g (as obtained by N_2 adsorption/desorption measurements). Second, to investigate whether or not the higher crystallinity/particle size of Co_9S_8@C leads to its higher catalytic activity, we prepared one more sample by heating the pristine Co_9S_8 (that was prepared hydrothermally at 200 °C) at 700 °C in N_2, and this material was denoted hereafter as Co_9S_8-700. Note that Co_9S_8@C was also prepared at 700 °C and Co_9S_8@C has a similar XRD pattern with Co_9S_8-700 (Figure S6 in the Supporting Information). Coupled with the catalytic results (Figure 6A) that show Co_9S_8@C has a better catalytic activity than Co_9S_8-700, we can conclude that Co_9S_8's crystallinity/particle size is not the reason behind the higher catalytic activity of Co_9S_8@C versus pristine Co_9S_8. Third, to further confirm the important role of Co_9S_8 in the catalytic activity of Co_9S_8@C, we synthesized Fe-based sulfide/carbon composite material (denoted as FeS@C) by using Fe^{3+} ions, in place of Co^{2+} ions under otherwise similar synthetic conditions with Co_9S_8@C, and then investigated its catalytic activity toward HER. The better catalytic activity of Co_9S_8@C (versus FeS@C), along with the fact that the two materials have similar structure of carbon matrix (Figure S7 in the Supporting Information), demonstrates the importance of Co_9S_8 nanoparticles for the catalytic activity of Co_9S_8@C. The above results clearly suggest that the Co_9S_8 nanoparticles are mainly responsible for the Co_9S_8's catalytic activity, with the carbon protection layer providing cooperative effects. The above results, coupled with the recent studies on carbon-protected cobalt nanoparticles for electrocatalysis,[21,22] also lead us to believe that the unique electronic interaction between Co_9S_8 and the carbon shell should be the reason behind the good catalytic activity of Co_9S_8@C. Nevertheless, further investigation may still be required to determine how the complicated interplay between Co_9S_8 and the carbon shell determines the catalytic efficiency of the composite material. Such theoretical studies are currently underway, and we hope to report on them in due course. Furthermore, some possible roles of the carbon layer in the composite material was also proposed as mentioned below. (i) The presence of the carbon layer in the Co_9S_8@C material can increase the conductivity of the composite material,[46] thus facilitating the electron transportation. (ii) The presence of N and S dopants in carbon might enhance the interaction between the material and the reactants (i.e., water).[21,22] (iii) The existence of N and S dopants could also decrease the work function of the carbon layer, thereby promoting the transfer of electrons from the carbon layer to reactants.[47] (iv) The carbon layer can protect the Co_9S_8 nanoparticles and improve the chemical and catalytic stabilities (see Figure 4G for chemical stability and see below for catalytic stability).

We further surveyed the literature to compare the HER activity in a neutral solution of Co_9S_8@C to other non-Pt relevant catalysts (see Table S1 in the Supporting Information). Heteroatom-doped and undoped MoS_x were reported to give a current density of 1 mA/cm^2 at overpotentials (η) of >200 mV,[19] whereas Co_9S_8@C only needs 150 mV to get the same current density. Co_9S_8@C has a catalytic activity that is much higher than a CoS microtube material (2.5 mA/cm^2 at η = 390 mV)[48] and is lower than an amorphous CoS_x film (10 mA/cm^2 at η = 160 mV).[20] However, this amorphous CoS_x film is unstable in acid solution and has a very low catalytic activity in

DOI: 10.1021/am507811a
ACS Appl. Mater. Interfaces 2015, 7, 980−988

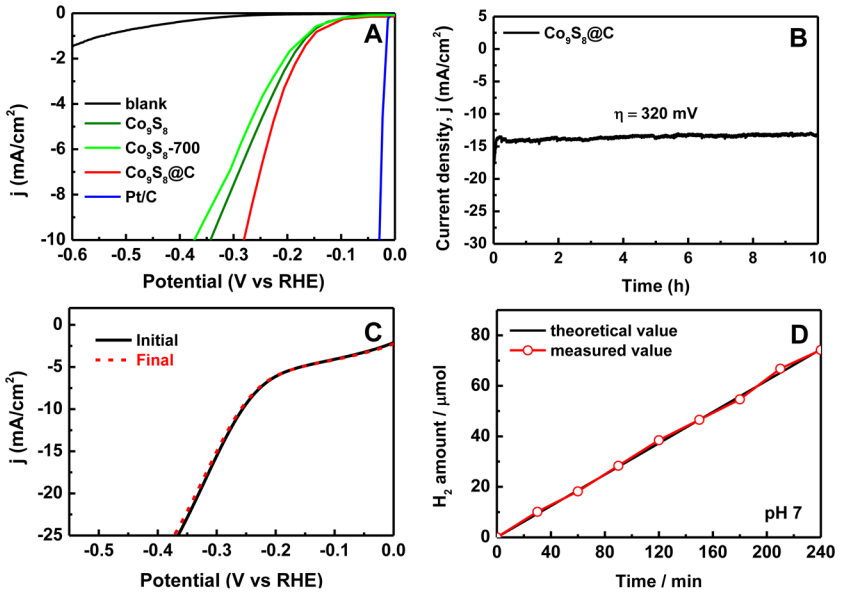

Figure 6. (A) Steady-state current densities as a function of the applied voltage in phosphate buffer (pH 7) without catalyst or with Co_9S_8@C, Co_9S_8, and Co_9S_8-700 as the electrocatalyst. (B) *I*–*t* curve obtained for HER with Co_9S_8@C at η = 320 mV at pH 7. (C) LSV curves obtained with Co_9S_8@C, before recycling (black curve) and 10 h after use under the *I*–*t* measurement shown in B (red curve). (D) Hydrogen production efficiency for HER under potentiostatic electrolysis with Co_9S_8@C at η = 320 mV at pH 7; The sample loading on the GCE is 0.28 mg/cm^2 in all the cases, and the obtained current densities are all normalized with the surface area of the GCE. To obtain the steady-state current densities, a dwell time of 5 min was applied at each voltage.

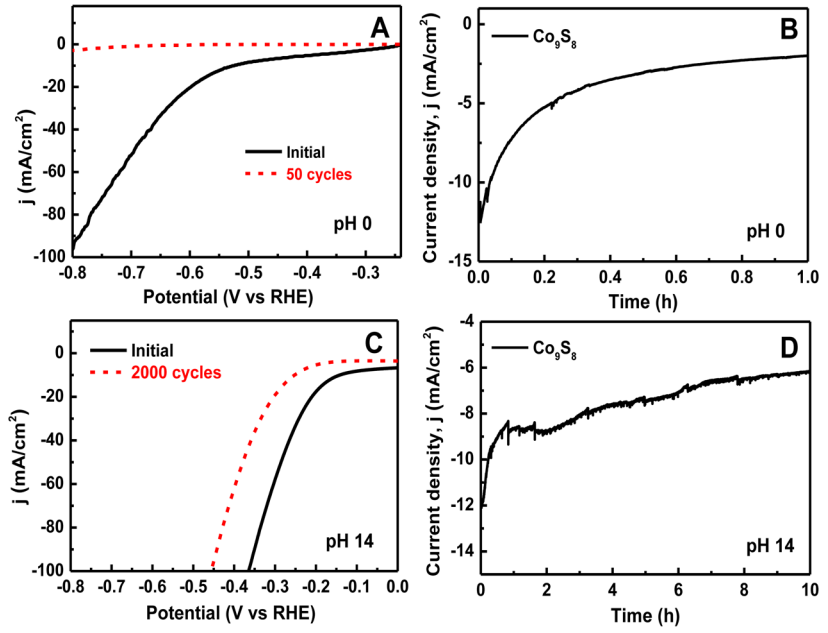

Figure 7. (A) Polarization curves for pristine Co_9S_8 before and after 50 CV cycles with a scan rate of 50 mV/s at pH 0. (B) *I*–*t* curve obtained for HER with Co_9S_8 at η = 260 mV at pH 0. (C) Polarization curves for pristine Co_9S_8 before and after 2000 CV cycles with a scan rate of 50 mV/s at pH 14. (D) *I*–*t* curve obtained for HER with Co_9S_8 at η = 220 mV at pH 14. The sample loading on the GCE is 0.28 mg/cm^2 in all the cases, and the obtained current densities are all normalized with the surface area of the GCE.

basic solution. Additionally, FeS nanoparticles were recently shown to give a current density of 1 mA/cm^2 at overpotential of ~1000 mV,[18] which is much larger than the value (150 mV) required by Co_9S_8@C. Furthermore, Co_9S_8@C exhibits a higher catalytic activity than some other active non-Pt HER catalysts, such as Mo_2C,[49] MoB,[49] heteroatom-doped nanocarbons,[21] and metallic cobalt@cobalt-oxo/hydroxo phosphate.[50] The above comparison demonstrates that our Co_9S_8@C material is a highly active catalyst for HER in neutral media.

Figure 6B depicts the current–time curve of the Co_9S_8@C-catalyzed hydrogen evolution reaction over 10 h at η = 320 mV at pH 7. The result shows that Co_9S_8@C retains its catalytic activity over this time. This was further confirmed by LSV curves (Figure 6C), which reveal that the Co_9S_8@C affords almost a similar LSV curve after a 10 h reaction time as before. Thus, it is concluded that Co_9S_8@C as electrocatalyst has an

DOI: 10.1021/am507811a
ACS Appl. Mater. Interfaces 2015, 7, 980–988

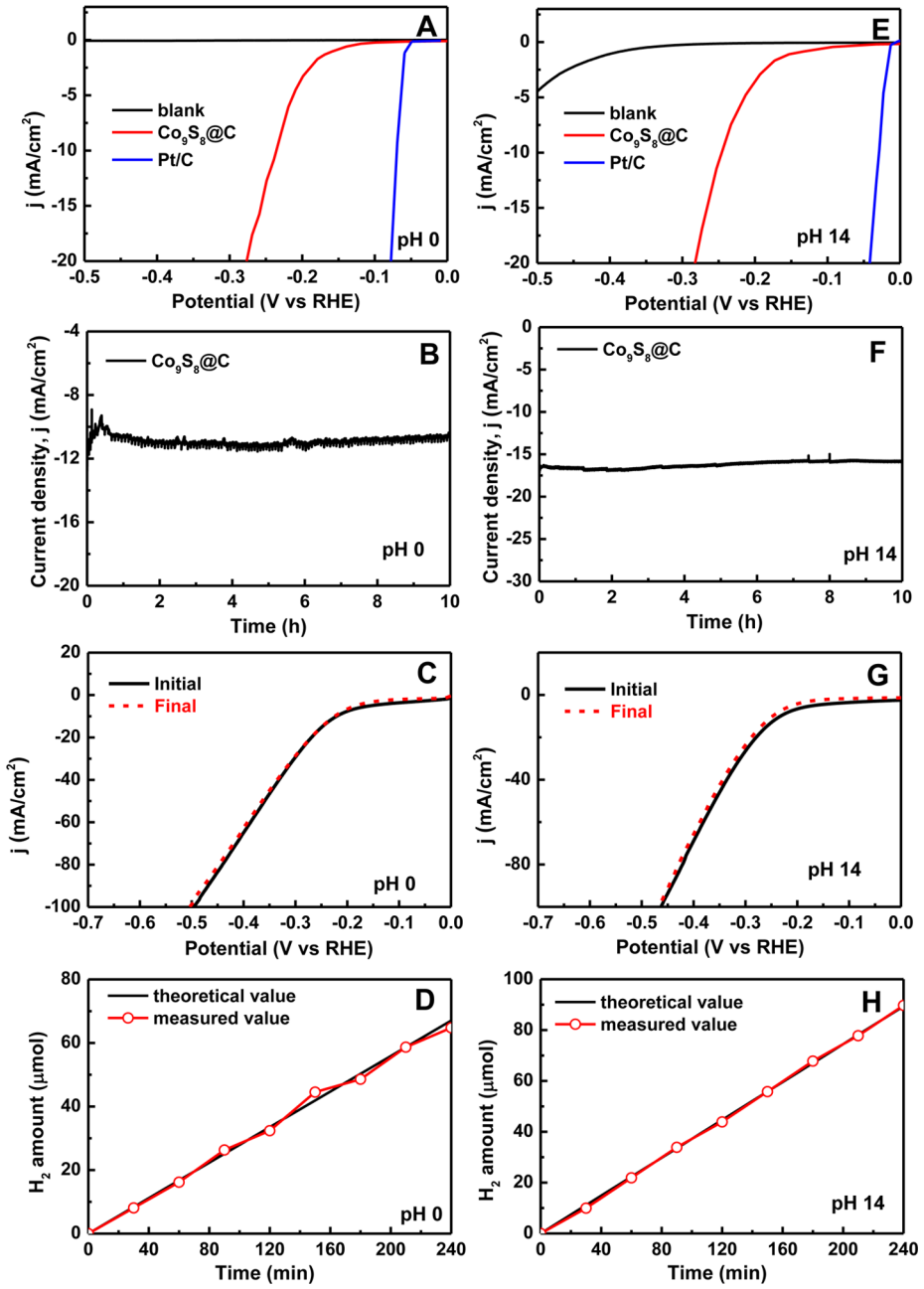

Figure 8. (A) Steady-state current densities as a function of the applied voltage at pH 0 with Co_9S_8@C. (B) *I*–*t* curve obtained for HER with Co_9S_8@C at η = 240 mV at pH 0. (C) LSV curves obtained with Co_9S_8@C, before recycling (black curve) and 10 h after use under the *I*–*t* measurement shown in B (red curve). (D) Hydrogen production efficiency for HER under potentiostatic electrolysis with Co_9S_8@C at η = 250 mV at pH 0. (E) Steady-state current densities as a function of the applied voltage at pH 14 with Co_9S_8@C. (F) *I*–*t* curve obtained for HER with Co_9S_8@C at η = 270 mV at pH 14. (G) LSV curves obtained with Co_9S_8@C, before recycling (black curve) and 10 h after use under the *I*–*t* measurement shown in F (red curve). (H) Hydrogen production efficiency for HER under potentiostatic electrolysis with Co_9S_8@C at η = 270 mV at pH 14. The sample loading on the GCE is 0.28 mg/cm^2 in all the cases, and the obtained current densities are all normalized with the surface area of the GCE. To obtain the steady-state current densities, a dwell time of 5 min was applied at each voltage.

excellent stability for HER at pH 7. Moreover, Co_9S_8@C gives nearly 100% Faradaic yield during HER in neutral solution because the experimentally detected H_2 amount is very close to the theoretical H_2 amount (Figure 6D).

It should be pointed out that the pristine Co_9S_8 material is catalytically stable for HER in neutral solution (Figure S8 in the Supporting Information). However, the catalytic activities of the pristine Co_9S_8 material at the pH extremes (pH 0 or 14) are quite unstable. As shown in Figure 7, the pristine Co_9S_8 material loses its catalytic activity quickly at pH 0 (Figure 7A,B), and its catalytic activity also falls into a decline at pH 14 (Figure 7C,D).

To overcome the limits of pristine Co_9S_8 and to illustrate the advantages of carbon-armored Co_9S_8 (i.e., Co_9S_8@C), we next studied the catalytic activity of Co_9S_8@C at the pH extremes (pH 0 or 14). As shown in Figure 8A,E, Co_9S_8@C exhibits obvious catalytic activities toward HER at both pH 0 and pH 14. Co_9S_8@C gives a current density of 10 mA/cm^2 at overpotentials of 240 and 250 mV at pH 0 and pH 14, respectively. Obviously, Co_9S_8@C exhibits a similar catalytic

DOI: 10.1021/am507811a
ACS Appl. Mater. Interfaces 2015, 7, 980–988

activity at the pH extremes (pH 0 or 14) with that in neutral media (pH 7). In contrast with pristine Co_9S_8 with poor stabilities in acidic and basic media, Co_9S_8@C has significant catalytic stabilities in both media. The potentiostatic HER in the presence of Co_9S_8@C was carried out for longer time periods under acidic (pH 0) or basic (pH 14) media. Figure 8B,F depicts the current−time curves of Co_9S_8@C-catalyzed HER over 10 h. After 10 h of the electrochemical reactions, there is barely any loss of catalytic activity in each media, demonstrating the excellent stability of Co_9S_8@C in HER at both pH values. These were also confirmed by LSV curves (Figure 8C,G), which show that the Co_9S_8@C affords almost similar LSV curves after a 10 h reaction time as before. In addition, Co_9S_8@C affords nearly 100% Faradaic yield during hydrogen evolution in the two cases (Figure 8D,H). These results, coupled with the high stability in neutral media, indicate Co_9S_8@C's great durability in HER under a wide pH range (pH 0−14). The above results also demonstrated that the carbon-armoring strategy should be quite effective for increasing the durability of some chemically unstable catalysts (e.g., Co_9S_8) over a wider pH range.

CONCLUSIONS

In summary, cobalt pentlandite (Co_9S_8) nanoparticles have been identified as an electrochemically active, noble-metal-free material toward hydrogen evolution reaction in neutral solution (pH 7). Furthermore, carbon-armored Co_9S_8 nanoparticles (Co_9S_8@C) are prepared by a facile method, and the resulting Co_9S_8@C material is proven to work well with high activity and 100% Faradaic yield at all pH values (pH 0−14). The simple preparation of Co_9S_8@C, its applicability over a wide pH window (pH 0−14), and its high catalytic activity bode well for the utilization of this material in a renewable water splitting technology. The carbon-armored catalyst reported here provides an example for creating low-cost, noble-metal-free water splitting catalysts with high efficiency and high durability in a wide pH range.

ASSOCIATED CONTENT

Supporting Information

XRD patterns of the samples obtained at 600 °C, 700 °C (i.e., Co_9S_8@C), and 800 °C. Raman spectrum of pure carbon material. TEM images of Co_9S_8@C. TEM images of Co_9S_8. GC result. XRD patterns of Co_9S_8@C and Co_9S_8-700. Structural characterization on FeS@C. Catalytic results of Co_9S_8 in neutral solution. This material is available free of charge via the Internet at http://pubs.acs.org.

AUTHOR INFORMATION

Corresponding Author

*E-mail: chemistryzouxx@gmail.com or xxzou@jlu.edu.cn.

Notes

The authors declare no competing financial interest.

ACKNOWLEDGMENTS

This work was supported by the NSFC (21371070, 21401066); the National Basic Research Program of China (2013CB632403); Jilin province science and technology development projects (20150520003JH, 20140101041JC, 20130204001GX); Graduate Innovation Fund of Jilin University (2014083).

REFERENCES

(1) Turner, J. A. Sustainable Hydrogen Production. *Science* **2004**, *305*, 972−974.
(2) Faber, M. S.; Jin, S. Earth-Abundant Inorganic Electrocatalysts and Their Nanostructures for Energy Conversion Applications. *Energy Environ. Sci.* **2014**, *7*, 3519−3542.
(3) Thoi, V. S.; Sun, Y.; Long, J. R.; Chang, C. J. Complexes of Earth-Abundant Metals for Catalytic Electrochemical Hydrogen Generation under Aqueous Conditions. *Chem. Soc. Rev.* **2013**, *42*, 2388−2400.
(4) Wang, M.; Chena, L.; Sun, L. Recent Progress in Electrochemical Hydrogen Production with Earth-Abundant Metal Complexes as Catalysts. *Energy Environ. Sci.* **2012**, *5*, 6763−6778.
(5) Hinnemann, B.; Moses, P. G.; Bonde, J.; Jørgensen, K. P.; Nielsen, J. H.; Horch, S.; Chorkendorff, I.; Nørskov, J. K. Biomimetic Hydrogen Evolution: MoS_2 Nanoparticles as Catalyst for Hydrogen Evolution. *J. Am. Chem. Soc.* **2005**, *127*, 5308−5309.
(6) Yang, Y.; Fei, H.; Ruan, G.; Xiang, C.; Tour, J. M. Edge-Oriented MoS_2 Nanoporous Films as Flexible Electrodes for Hydrogen Evolution Reactions and Supercapacitor Devices. *Adv. Mater.* **2014**, DOI: 10.1002/adma.201402847.
(7) Zhu, H.; Du, M.; Zhang, M.; Zou, M.; Yang, T.; Fu, Y.; Yao, J. The Design and Construction of 3D Rose-Petalshaped MoS_2 Hierarchical Nanostructures with Structure-Sensitive Properties. *J. Mater. Chem. A* **2014**, *2*, 7680.
(8) Yan, Y.; Xia, B. Y.; Xu, Z.; Wang, X. Recent Development of Molybdenum Sulfides as Advanced Electrocatalysts for Hydrogen Evolution Reaction. *ACS Catal.* **2014**, *4*, 1693−1705.
(9) Wang, H.; Lu, Z.; Kong, D.; Sun, J.; Hymel, T. M.; Cui, Y. Electrochemical Tuning of MoS_2 Nanoparticles on Three-Dimensional Substrate for Efficient Hydrogen Evolution. *ACS Nano* **2014**, *8*, 4940−4947.
(10) Kibsgaard, J.; Chen, Z.; Reinecke, B. N.; Jaramillo, T. F. Engineering the Surface Structure of MoS_2 to Preferentially Expose Active Edge Sites for Electrocatalysis. *Nat. Mater.* **2012**, *11*, 963−969.
(11) Voiry, D.; Yamaguchi, H.; Li, J.; Silva, R.; Alves, D. C. B.; Fujita, T.; Chen, M.; Asefa, T.; Shenoy, V. B.; Eda, G.; Chhowalla, M. Enhanced Catalytic Activity in Strained Chemically Exfoliated WS_2 Nanosheets for Hydrogen Evolution. *Nat. Mater.* **2013**, *12*, 850−855.
(12) Yang, J.; Voiry, D.; Ahn, S. J.; Kang, D.; Kim, A. Y.; Chhowalla, M.; Shin, H. S. Two-Dimensional Hybrid Nanosheets of Tungsten Disulfide and Reduced Graphene Oxide as Catalysts for Enhanced Hydrogen Evolution. *Angew. Chem., Int. Ed.* **2013**, *52*, 13751−13754.
(13) Faber, M. S.; Dziedzic, R.; Lukowski, M. A.; Kaiser, N. S.; Ding, Q.; Jin, S. High-Performance Electrocatalysis Using Metallic Cobalt Pyrite (CoS_2) Micro- and Nanostructures. *J. Am. Chem. Soc.* **2014**, *136*, 10053−10061.
(14) Faber, M. S.; Lukowski, M. A.; Ding, Q.; Kaiser, N. S.; Jin, S. Earth-Abundant Metal Pyrites (FeS_2, CoS_2, NiS_2, and Their Alloys) for Highly Efficient Hydrogen Evolution and Polysulfide Reduction Electrocatalysis. *J. Phys. Chem. C* **2014**, *118*, 21347−21356.
(15) Kong, D. S.; Cha, J. J.; Wang, H. T.; Lee, H. R.; Cui, Y. First-Row Transition Metal Dichalcogenide Catalysts for Hydrogen Evolution Reaction. *Energy Environ. Sci.* **2013**, *6*, 3553−3558.
(16) Kong, D. S.; Wang, H. T.; Lu, Z. Y.; Cui, Y. $CoSe_2$ Nanoparticles Grown on Carbon Fiber Paper: An Efficient and Stable Electrocatalyst for Hydrogen Evolution Reaction. *J. Am. Chem. Soc.* **2014**, *136*, 4897−4900.
(17) Xu, Y.-F.; Gao, M.-R.; Zheng, Y.-R.; Jiang, J.; Yu, S.-H. Nickel/Nickel(II) Oxide Nanoparticles Anchored onto Cobalt(IV) Diselenide Nanobelts for the Electrochemical Production of Hydrogen. *Angew. Chem., Int. Ed.* **2013**, *52*, 8546−8550.
(18) Giovanni, C. D.; Wang, W.-A.; Nowak, S.; Grenèche, J.-M.; Lecoq, H.; Mouton, L.; Giraud, M.; Tard, C. Bioinspired Iron Sulfide Nanoparticles for Cheap and Long-Lived Electrocatalytic Molecular Hydrogen Evolution in Neutral Water. *ACS Catal.* **2014**, *4*, 681−687.
(19) Merki, D.; Fierro, S.; Vrubel, H.; Hu, X. Amorphous Molybdenum Sulfide Films as Catalysts for Electrochemical Hydrogen Production in Water. *Chem. Sci.* **2011**, *2*, 1262.

DOI: 10.1021/am507811a
ACS Appl. Mater. Interfaces 2015, 7, 980−988

(20) Sun, Y. J.; Liu, C.; Grauer, D. C.; Yano, J.; Long, J. R.; Yang, P.; Chang, C. J. Electrodeposited Cobalt-Sulfide Catalyst for Electrochemical and Photoelectrochemical Hydrogen Generation from Water. *J. Am. Chem. Soc.* **2013**, *135*, 17699−17702.
(21) Zou, X.; Huang, X.; Goswami, A.; Silva, R.; Sathe, B. R.; Mikmeková, E.; Asefa, T. Cobalt-Embedded Nitrogen-Rich Carbon Nanotubes Efficiently Catalyze Hydrogen Evolution Reaction at All pH Values. *Angew. Chem., Int. Ed.* **2014**, *53*, 4372−4376.
(22) Gao, S.; Li, G.-D.; Liu, Y.; Chen, H.; Feng, L.-L.; Wang, Y.; Yang, M.; Wang, D.; Wang, S.; Zou, X. Electrocatalytic H_2 Production from Seawater over Co, N-Codoped Nanocarbons. *Nanoscale* **2014**, DOI: 10.1039/c4nr04924a.
(23) Hambourger, M.; Gervaldo, M.; Svedruzic, D.; King, P. W.; Gust, D.; Ghirardi, M.; Moore, A. L.; Moore, T. A. [FeFe]-Hydrogenase-Catalyzed H_2 Production in a Photoelectrochemical Biofuel Cell. *J. Am. Chem. Soc.* **2008**, *130*, 2015−2022.
(24) Le Goff, A.; Artero, V.; Jousselme, B.; Tran, P. D.; Guillet, N.; Métayé, R.; Fihri, A.; Palacin, S.; Fontecave, M. From Hydrogenases to Noble Metal-Free Catalytic Nanomaterials for H_2 Production and Uptake. *Science* **2009**, *326*, 1384−1387.
(25) Kundu, A.; Sahu, J. N.; Redzwan, G.; Hashim, M. A. An Overview of Cathode Material and Catalysts Suitable for Generating Hydrogen in Microbial Electrolysis Cell. *Int. J. Hydrogen Energy* **2013**, *38*, 1745−1757.
(26) Leroy, R. L. Industrial Water Electrolysis: Present and Future. *Int. J. Hydrogen Energy* **1983**, *8*, 401−417.
(27) Bezverkhyy, I.; Afanasiev, P.; Danot, M. Preparation of Highly Dispersed Pentlandites $(M,M')_9S_8$ (M, M′ = Fe, Co, Ni) and Their Catalytic Properties in Hydrodesulfurization. *J. Phys. Chem. B* **2004**, *108*, 7709−7715.
(28) Hoodless, R. C.; Moyes, R. B.; Wells, P. B. D-Tracer Study of Butadiene Hydrogenation and Tetrahydrothiophen Hydrodesulphurisation Catalysed by Co_9S_8. *Catal. Today* **2006**, *114*, 377−382.
(29) Sidik, R. A.; Anderson, A. B. Co_9S_8 as a Catalyst for Electroreduction of O_2: Quantum Chemistry Predictions. *J. Phys. Chem. B* **2006**, *110*, 936−941.
(30) Vayner, E.; Sidik, R. A.; Anderson, A. B. Experimental and Theoretical Study of Cobalt Selenide as a Catalyst for O_2 Electroreduction. *J. Phys. Chem. B* **2007**, *111*, 10508−10513.
(31) Guo, W.; Chen, C.; Ye, M.; Lv, M.; Lin, C. Carbon Fiber/Co_9S_8 Nanotube Arrays Hybrid Structures for Flexible Quantum Dot-Sensitized Solar Cells. *Nanoscale* **2014**, *6*, 3656−3663.
(32) Chang, S.-H.; Lu, M.-D.; Tung, Y.-L.; Tuan, H.-Y. Gram-Scale Synthesis of Catalytic Co_9S_8 Nanocrystal Ink as a Cathode Material for Spray-Deposited, Large Area Dye-Sensitized Solar Cells. *ACS Nano* **2013**, *7*, 9443−9451.
(33) Chen, H.-W.; Kung, C.-W.; Tseng, C.-M.; Wei, T.-C.; Sakai, N.; Morita, S.; Ikegami, M.; Miyasaka, T.; Ho, K.-C. Plastic Based Dye-Sensitized Solar Cells Using Co_9S_8 Acicular Nanotube Arrays as the Counter Electrode. *J. Mater. Chem. A* **2013**, *1*, 13759−13768.
(34) Wang, G.; Zhuo, S. Hierarchical Micro/Nano-Structured Cobalt Sulphide Spindles as Low-Cost Counter Electrodes for Dye-Sensitized Solar Cells. *Phys. Chem. Chem. Phys.* **2013**, *15*, 13801−13804.
(35) Xu, J.; Wang, Q.; Wang, X.; Xiang, Q.; Liang, B.; Chen, D.; Shen, G. Flexible Asymmetric Supercapacitors Based upon Co_9S_8 Nanorod// Co_3O_4@RuO_2 Nanosheet Arrays on Carbon Cloth. *ACS Nano* **2013**, *7*, 5453−5426.
(36) Ramachandran, R.; Saranya, M.; Santhosh, C.; Velmurugan, V.; Raghupathy, B. P. C.; Jeong, S. K.; Grace, A. N. Co_9S_8 Nanoflakes on Graphene (Co_9S_8/G) Nanocomposites for High Performance Supercapacitors. *RSC Adv.* **2014**, *4*, 21151−21162.
(37) Qin, W.; Hu, B.; Bao, D.; Gao, P. The Preparation of Co_9S_8 and CoS_2 Nanoparticles by a High Energy Ball-Milling Method and Their Electrochemical Hydrogen Storage Properties. *Int. J. Hydrogen Energy* **2014**, *39*, 9300−9306.
(38) Shi, W.; Zhu, J.; Rui, X.; Cao, X.; Chen, C.; Zhang, H.; Hng, H. H.; Yan, Q. Controlled Synthesis of Carbon-Coated Cobalt Sulfide Nanostructures in Oil Phase with Enhanced Li Storage Performances. *ACS Appl. Mater. Interfaces* **2012**, *4*, 2999−3006.
(39) Ko, Y. N.; Choi, S. H.; Park, S. B.; Kang, Y. C. Preparation of Yolk-Shell and Filled Co_9S_8 Microspheres and Comparison of Their Electrochemical Properties. *Chem.—Asian J.* **2014**, *9*, 572−576.
(40) Zhou, Y.-X.; Yao, H.-B.; Wang, Y.; Liu, H.-L.; Gao, M.-R.; Shen, P.-K.; Yu, S.-H. Hierarchical Hollow Co_9S_8 Microspheres: Solvothermal Synthesis, Magnetic, Electrochemical, and Electrocatalytic Properties. *Chem.—Eur. J.* **2010**, *16*, 12000−12007.
(41) Jin, R.; Liu, J.; Xu, Y.; Li, G.; Chen, G. Solvothermal Synthesis and Excellent Electrochemical Performance of Polycrystalline Rose-Like Co_9S_8 Hierarchical Architectures. *J. Mater. Chem. A* **2013**, *1*, 7995−7999.
(42) Wang, Z.; Pan, L.; Hu, H.; Zhao, S. Co_9S_8 Nanotubes Synthesized on the Basis of Nanoscale Kirkendall Effect and Their Magnetic and Electrochemical Properties. *CrystEngComm* **2010**, *12*, 1899−1904.
(43) Yin, P.-F.; Sun, L.-L.; Gao, Y.-L.; Wang, S.-Y. Preparation and Characterization of Co_9S_8 Nanocrystalline and Nanorods. *Bull. Mater. Sci.* **2008**, *31*, 593−596.
(44) Zhang, B.-X.; Gao, H.; Li, X.-L. Synthesis and Optical Properties of Nitrogen and Sulfur Co-Doped Graphene Quantum Dots. *New J. Chem.* **2014**, *38*, 4615−4621.
(45) Wu, G.; Chung, H. T.; Nelson, M.; Artyushkova, K.; More, K. L.; Johnston, C. M.; Zelenay, P. Graphene-Riched Co_9S_8-N-C Non-Precious Metal Catalyst for Oxygen Reduction in Alkaline Media. *ECS Trans.* **2011**, *41*, 1709−1717.
(46) Mai, L.; Li, S.; Dong, Y.; Zhao, Y.; Luo, Y.; Xu, H. Long-Life and High-Rate $Li_3V_2(PO_4)_3$/C Nanosphere Cathode Materials with Three-Dimensional Continuous Electron Pathways. *Nanoscale* **2013**, *5*, 4864−4869.
(47) Cheon, J. Y.; Kim, J. H.; Kim, J. H.; Goddeti, K. C.; Park, J. Y.; Joo, S. H. Intrinsic Relationship between Enhanced Oxygen Reduction Reaction Activity and Nanoscale Work Function of Doped Carbons. *J. Am. Chem. Soc.* **2014**, *136*, 8875−8878.
(48) Lin, C.-Y.; Mersch, D.; Jefferson, D. A.; Reisner, E. Cobalt Sulphide Microtube Array as Cathode in Photoelectrochemical Water Splitting with Photoanodes. *Chem. Sci.* **2014**, *5*, 4906−4913.
(49) Vrubel, H.; Hu, X. Molybdenum Boride and Carbide Catalyze Hydrogen Evolution in Both Acidic and Basic Solutions. *Angew. Chem., Int. Ed.* **2012**, *51*, 12875−12878.
(50) Cobo, S.; Heidkamp, J.; Jacques, P.-A.; Fize, J.; Fourmond, V.; Guetaz, L.; Jousselme, B.; Ivanova, V.; Dau, H.; Palacin, S.; Fontecave, M.; Artero, V. A Janus Cobalt-Based Catalytic Material for Electro-Splitting of Water. *Nat. Mater.* **2012**, *11*, 802−807.

DOI: 10.1021/am507811a
ACS Appl. Mater. Interfaces 2015, 7, 980−988